Electronic Supplementary Material (ESI) for Reaction Chemistry & Engineering.

Supplementary Information

Selective formation of propan-1-ol from propylene *via* a chemical looping approach

A.R.P. Harrison [a]*, E.J. Marek [a]*

[a] Department of Chemical Engineering and Biotechnology, University of Cambridge,
Philippa Fawcett Drive, Cambridge, CB3 0AS, United Kingdom

* Corresponding authors: arph2@cam.ac.uk, ejm94@cam.ac.uk

S1. Schematic diagram of experimental rig

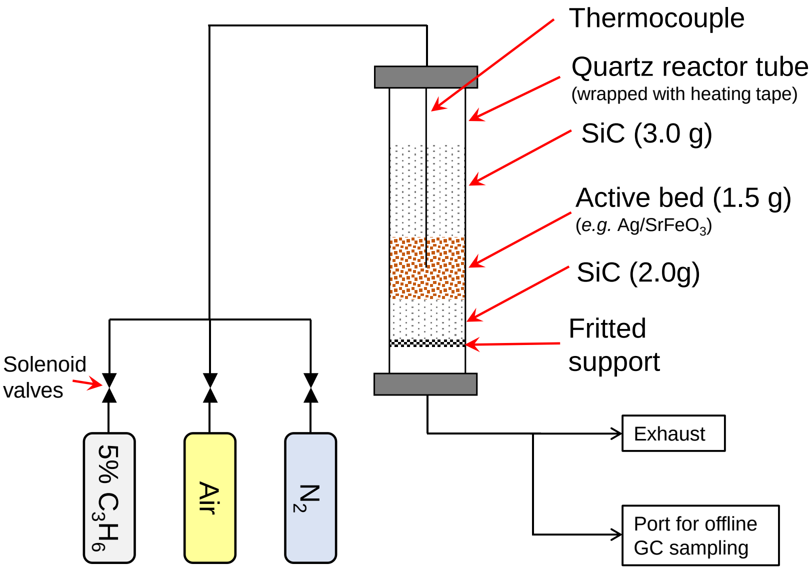

Figure S1: Schematic diagram showing arrangement of experimental rig. Not to scale.

S2. Use of Owlstone V-OVG to generate calibration vapour mixtures

To generate low concentration (~1000ppm) vapour mixtures of C_3 analytes for calibration and catalytic experiments, an Owlstone V-OVG vapour generator was used. A ~2.5-3 g liquid sample of analyte was loaded into a stainless steel diffusion tube, and weighed before starting measurements. The tube was then inserted into the heated chamber of the vapour generator, with N_2 purge flow set to 220 mL/min. For calibration purposes, 10 mL vapour samples were taken from the outlet gas stream and injected into the GC inlet, and simultaneously the diffusion tube was removed and weighed. The average vapour concentration was then calculated used:

$$C = 10^{12} \cdot \frac{RT}{P} \cdot \frac{1}{qM_r} \cdot \frac{dm}{dt} \qquad \textbf{[Eq. S1]}$$

where *C* is the analyte concentration (ppm), *R* is the molar gas constant (J/mol K), *T* is the chamber temperature (K), *P* is the chamber pressure (Pa), *q* is the nitrogen flowrate (mL/min), M_r is the molar mass of the analyte (g/mol), and *dm/dt* is the rate of change of sample mass (g/min). For catalytic experiments, the outlet gas from the vapour generator was connected to the reactor inlet, without removing the diffusion tube over the course of the experiment. Example measurements showing sample mass as a function of time are given in Fig. S2.

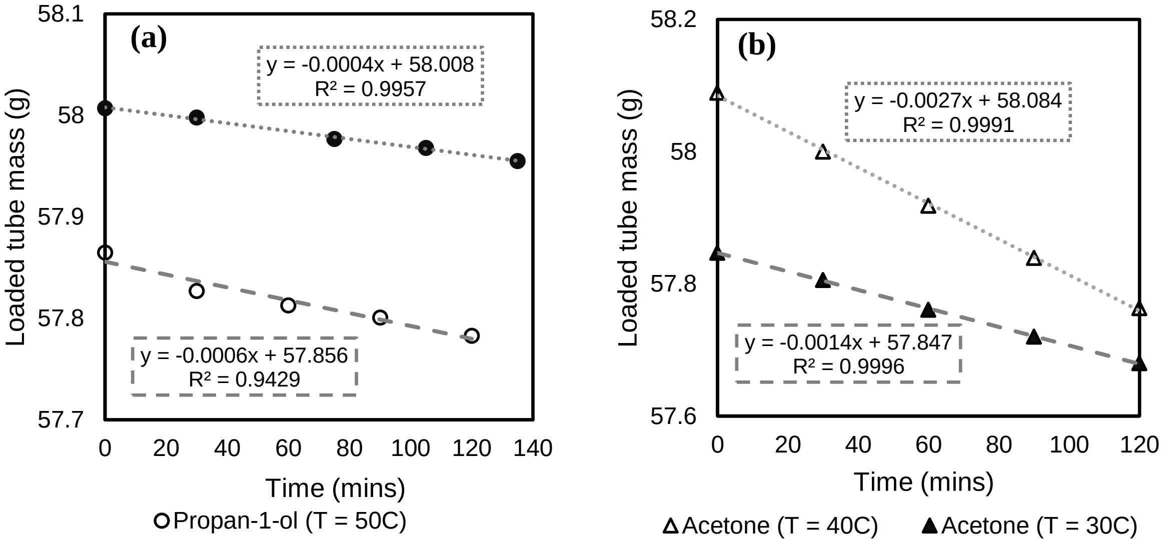

Figure S2: Example graphs showing total mass (diffusion tube plus analyte liquid mass) as a function of time for propan-1-ol (a) and acetone (b). Linear gradient implies approximately constant outlet analyte concentration.

S3. X-ray diffraction patterns for supported catalysts.

Table S1: ICSD reference patterns used for XRD refinement

Phase	**ICSD Collection Code**
$SrFeO_3$	91062
SrO	163625
$Sr_3Fe_2O_7$	74437
$SrCO_3$	15195
Ag	53759
Au	52249
AgCl	56538
AgAu	604769
γ-Al_2O_3	173014
δ-Al_2O_3	40200

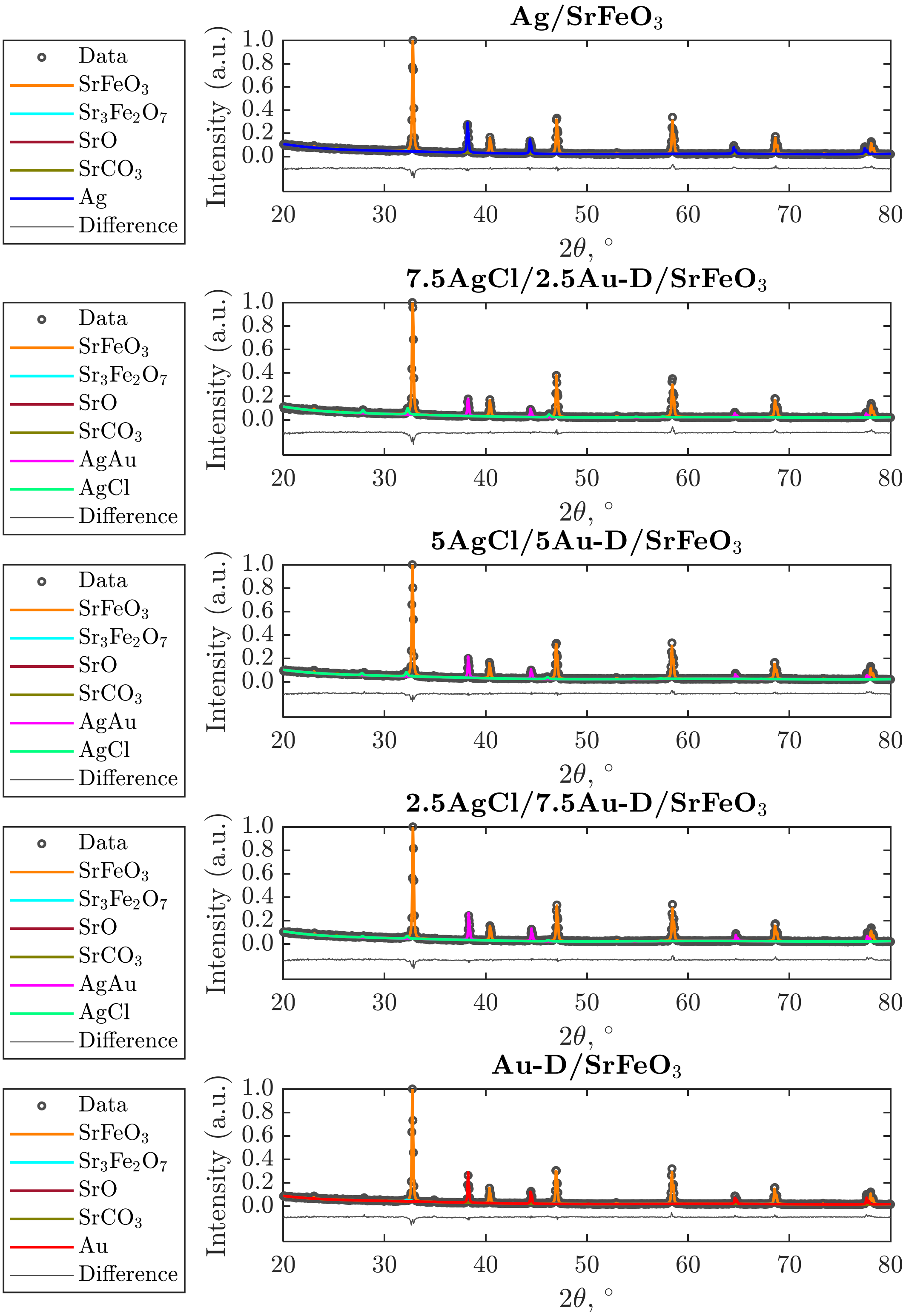

Figure S3: XRD patterns for Ag/SrFeO$_3$, Au/SrFeO$_3$, and *x*Ag/(*10-x*)Au-D/SrFeO$_3$ catalysts, with peaks identified.

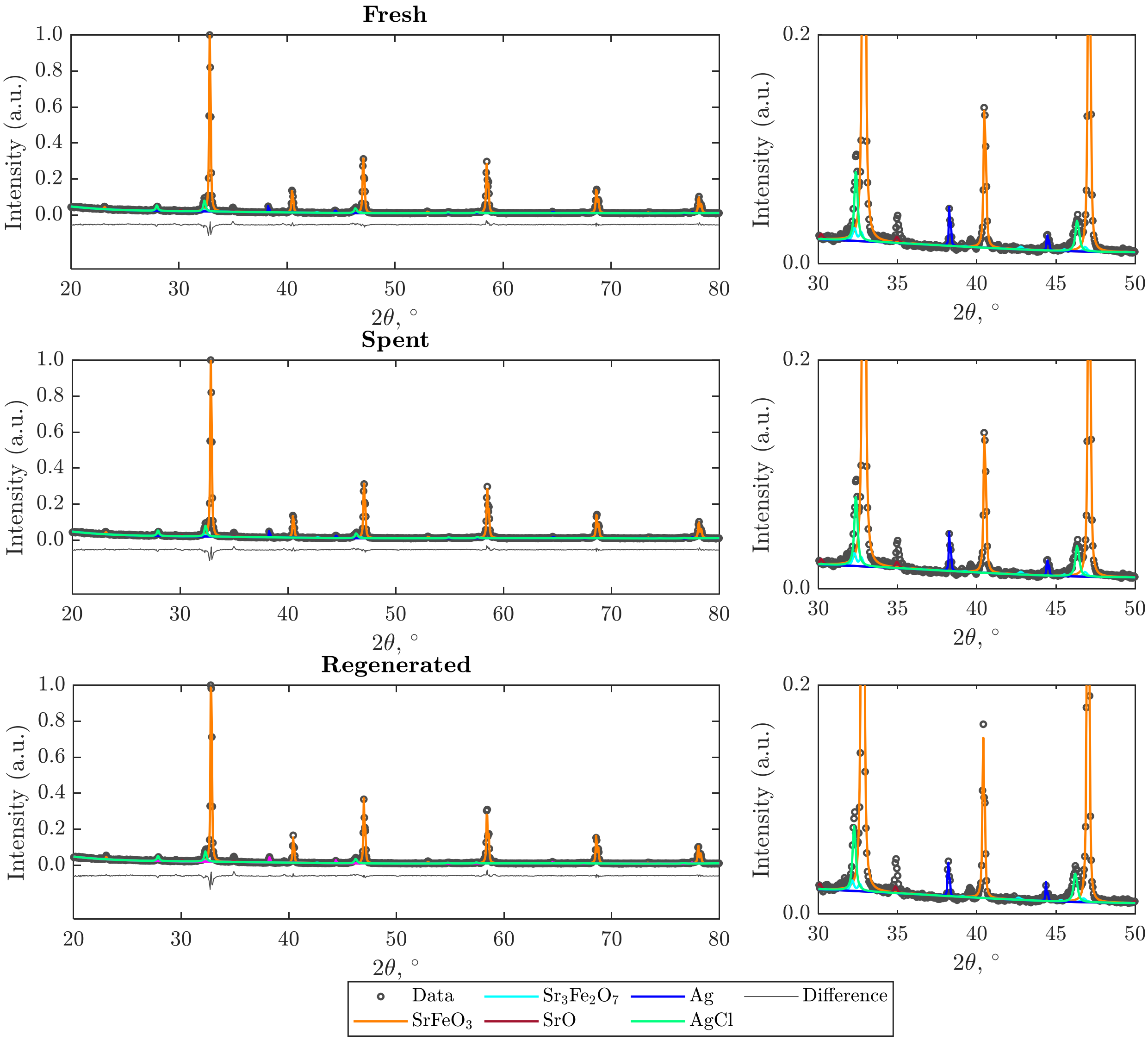

Figure S4: XRD patterns for fresh, spent, and regenerated AgCl/$SrFeO_3$, with AgCl peaks indicated. Spent sample was withdrawn from reactor tube after 15 chemical looping cycles. The regenerated sample was produced by heating the spent sample to 650°C in air for 5 hours, followed by cooling in air to room temperature.

Table S2: Phase quantification *via* XRD for $SrFeO_3$ support and impregnated samples. Compositions in wt%. For phase quantification, metallic Ag, metallic Au and AgAu alloy cannot be unambiguously distinguished due to the closeness of the peaks to each other.

	$SrFeO_3$	**Ag/$SrFeO_3$**	**7.5AgCl/2.5Au-D/$SrFeO_3$**	**5AgCl/5Au-D/$SrFeO_3$**	**2.5AgCl/7.5Au-D/$SrFeO_3$**	**Au-D/$SrFeO_3$**
Ag	-	11.8	-	-	-	-
AgCl	-	-	6.9	5.1	3.4	-
Au	-	-	-	-	-	7.3
AgAu	-	-	5.1	6.0	7.9	-
$SrFeO_3$	96.0	84.0	84.0	85.0	85.0	87.0

$Sr_3Fe_2O_7$	2.0	2.0	0.7	2.0	1.0	3.0
SrO	0.1	0.0	0.3	0.1	0.1	0.6
$SrCO_3$	1.5	3.0	3.0	2.0	3.0	2.1

	AgCl/$SrFeO_3$	**Ag-AgCl/Au-H/$SrFeO_3$**	**Ag/Au-L/$SrFeO_3$**
Ag	1.1	**-**	-
AgCl	8.8	3.4	-
Au	-	-	-
AgAu	-	5.1	4.6
$SrFeO_3$	85.0	90.0	92.0
$Sr_3Fe_2O_7$	3.0	0.0	1.0
SrO	0.8	0.3	0.0
$SrCO_3$	1.3	1.5	2.0

Mean crystallite size was determined for Ag, AgCl, Au, and AgAu from the XRD patterns for Ag/$SrFeO_3$, AgCl/$SrFeO_3$, Au-D/$SrFeO_3$, and 5AgCl/5Au-D/$SrFeO_3$ using the Scherrer equation[1]:

$$\tau = \frac{K\lambda}{\beta \cos\theta} \qquad \textbf{[Eq. S2]}$$

where τ is the mean crystallite size (nm), K is a dimensionless shape factor (taken to be ~K = 0.9), λ is the X-ray wavelength (0.15406 nm), β is the full width at half maximum (radians), and θ is the Bragg angle (radians).

Table S3: Mean crystallite size (nm) of Ag, AgCl, Au, and AgAu, estimated from broadening of three XRD peaks for each phase.

	Ag/$SrFeO_3$	**AgCl/$SrFeO_3$**	**Au-D/$SrFeO_3$**	**5AgCl/5Au-D/$SrFeO_3$**
Ag	50.2 ± 6.6	79.9 ± 15.9	-	-
AgCl	-	30.0 ± 3.2	-	31.9 ± 2.1
AgAu	-	-	-	-
Au	-	-	68.0 ± 3.4	75.5 ± 4.3

S4. Additional STEM-EDS surface maps for 5AgCl/5Au-D/SrFeO$_3$ sample

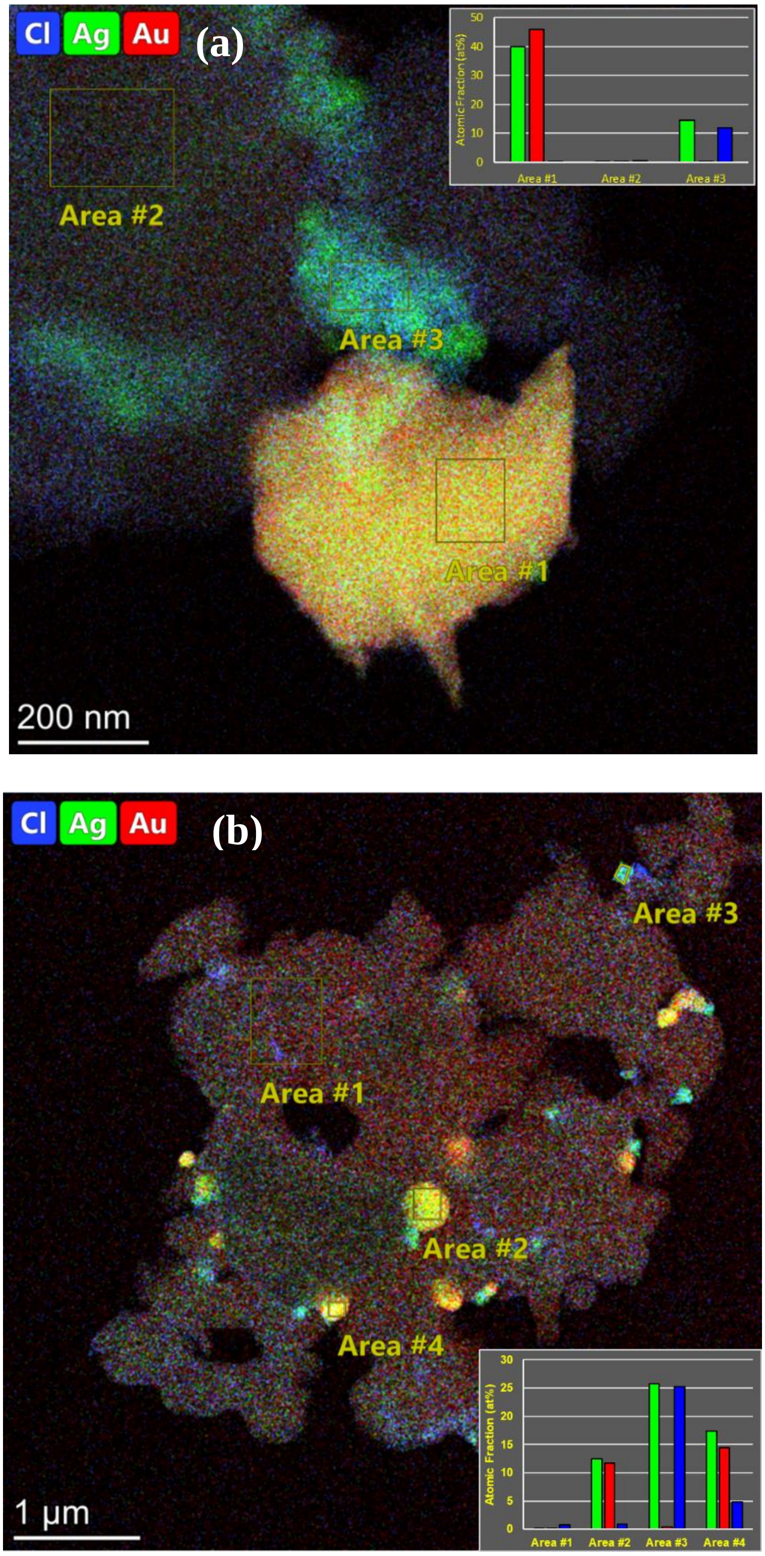

Figure S5: STEM-EDS surface maps of 5AgCl/5Au-D/SrFeO$_3$ sample, with elemental composition of areas of interest given in inlay. In **(a)**, particles of AgCl (areas 3 and 4) show an Ag:Cl ratio of ~2, suggesting the presence of metallic Ag within the particles, whereas the AgCl particles in **(b)** (area 3) show a ratio of approximately 1, suggesting a pure AgCl phase.

S5. XPS analysis of Ag/$SrFeO_3$, AgCl/$SrFeO_3$, and 5AgCl/5Au-D/$SrFeO_3$ samples

To further identify the surface species present in the catalyst samples, XPS measurements were conducted for Ag/$SrFeO_3$, AgCl/$SrFeO_3$, and 5AgCl/5Au-D/$SrFeO_3$ samples. The experimental measurements, and fitted peaks, are shown in Fig. 4, with binding energy (BE) values for each peak given in Table S4.

The Ag foil standard measured (Fig. 4a) shows a single main peak for each of the Ag $3d_{5/2}$ and Ag $3d_{7/2}$ binding energy levels. The binding energy measured for Ag $3d_{5/2}$ was 368.2 eV, which is consistent with literature value for metallic Ag^0 [2]. The binding energy of Ag $3d_{5/2}$ measured for the Ag/$SrFeO_3$ shows a minimal shift with respect to the Ag^0 reference value (<0.1 eV). The AgCl standard used shows a single peak at 367.9 eV, corresponding to a peak shift with respect to metallic Ag^0 of -0.35 eV, which is consistent with the expected value for the shift between Ag^0 and Ag(I) in AgCl [3].

The XPS spectra for AgCl/SrFeO3 and 5AgCl/5Au-D/$SrFeO_3$ each show two distinct Ag $3d_{5/2}$ features. The AgCl/$SrFeO_3$ spectrum shows main peaks at 367.8 (assigned to AgCl), and 369.0 eV, which is assigned to strongly oxidised Ag species, as reported by Lu and co-workers for 10% NaCl-promoted Ag [4]. The peak at 369.0 eV may therefore correspond to Ag^+ species in contact with $O_{lattice}$ in the $SrFeO_3$ support, or with strongly adsorbed O_a adatoms. The peak at 369.0 eV alternatively may correspond to AgO_x species, as the binding energy is within the reported range for silver oxides [5].

For 5AgCl/5Au-D/$SrFeO_3$, two main Ag $3d_{5/2}$ peaks at 367.4 eV and 368.6 eV were detected. As AgCl and AgAu are known to be present at the surface as distinct phases from STEM analyses, the peak at 367.4 eV was assigned to Ag(I) in AgCl, and the peak at 368.6 eV was assigned to Ag^0 in particles AgAu alloy. The peak shift of ~+0.4 eV with respect to the Ag standard for AgAu is within the range reported in previous literature studies of AgAu alloy nanoparticles [6,7] .

The fitted peaks for Au $4f_{7/2}$ for the Au foil standard, and 5AgCl/5Au-D/$SrFeO_3$ are shown in Figure 4b. The Au foil standard shows a single peak, set to 84.0 eV[2].

The 5AgCl/5Au-D/$SrFeO_3$ sample shows two distinct peaks at 84.5 eV and 85.5 eV. Malathi and co-workers [7]) report a shift of *c.*+1 eV (with respect to an Au^0 metallic standard, *i.e.* to 85 eV) for AgAu nanoparticles, which is approximately consistent with the spacing between the two major peaks for 5AgCl/5Au-D/$SrFeO_3$. Other studies [8,9] also report a positive BE shift for Au $4f_{7/2}$ in AgAu alloy nanoparticles, but with smaller magnitude (*c.*+0.2 eV). Therefore, the smaller peak at 84.5 eV is assigned to Au^0 in a local environment of Au, and the larger peak at 85.5 eV is assigned to Au^0 in AgAu alloy (*i.e.* in contact with Ag^0). The observed difference in Au electronic states was possibly due to heterogeneity within single ~200 nm AgAu particles, as no Au-only particles were detected from STEM-EDS composition maps (shown in Fig. 3 of main manuscript). The source of the +0.5 eV overall shift of the Au^0 peak with respect to the metallic standard is unknown, but may be due to interaction between the Au particle and the oxide support.

The O 1s spectra for each oxide sample are shown in Fig. 4c. The spectra for $AgCl/SrFeO_3$ and $5AgCl/5Au-D/SrFeO_3$ show two main oxygen features, at ~530.3-530.4 eV, and ~532.2-532.3 eV. The O 1s peaks may be assigned to lattice oxygen, and surface carbonate/hydroxide species respectively [10,11]. An additional peak at 529.5 eV is also detected for the $Ag/SrFeO_3$ sample, which may be assigned to Ag_2O or AgO [12,13]. The absence of this peak in the $AgCl/SrFeO_3$ and $5AgCl/5Au-D/SrFeO_3$ spectra is not surprising, as Ag is known from XRD and STEM-EDS to be primarily present as AgCl, and so surface silver oxides are not expected to be present. In the O 1s XPS spectra for $Ag/SrFeO_3$ and $AgCl/SrFeO_3$, a small feature is also observed at 533.6-533.8 eV, which is attributed to adsorbed surface oxygen[14]. The +0.2 eV shift between AgCl and Ag is therefore consistent with the hypothesis that the presence of Cl makes surface oxygen more electrophilic [15] , as an increase in binding energy corresponds to a stronger attraction to available electrons.

The Cl 2p spectra for each sample are shown in Fig. 4d. For the $Ag/SrFeO_3$ sample, no chloride peaks were detected, as expected. The lack of chloride therefore confirms that the $SrCO_3$, Fe_2O_3 and $AgNO_3$ precursors used to produce the catalyst can be taken to be chloride-free, and therefore that any chloride species detected on the surface of other samples must be due to treatment with HCl (in the case of $AgCl/SrFeO_3$) or $AuCl_3$ (for $5AgCl/5Au-D/SrFeO_3$). The AgCl standard and $AgCl/SrFeO_3$ samples show a Cl $2p_{3/2}$ peak at 198.8 eV, and $2p_{3/2}$-$2p_{1/2}$ peak separation of c.1.6 eV, in good agreement with literature [13]. A peak shift of c.-1.5 eV between the $2p_{3/2}$ AgCl standard and the $AgCl/SrFeO_3$ sample was observed, which is similar to the shift reported for thin layers (~5 nm) of AgCl in contact with Ag [16]. The 5AgCl/5Au-D/$SrFeO_3$ sample shows a single Cl $2p_{3/2}$ peak at 199.1 eV, which corresponds to a slight positive shift of *c.*+0.3 eV with respect to the AgCl standard.

Table S4: XPS deconvolution peak positions for standards and catalyst samples.

Sample	**Ag 3d$_{5/2}$ BE values (eV)**	**Au 4f$_{7/2}$ BE values (ev)**	**Cl 2p$_{3/2}$ BE values (ev)**	**O 1s BE values (ev)**
Ag standard	368.2	-	-	-
AgCl standard	367.9	-	198.8, 200.5	-
Au standard	-	84.00†	-	-
Ag/$SrFeO_3$	368.2	-	-	528.3, 529.5, 530.8
AgCl/$SrFeO_3$	367.8, 369.0,	-	197.3, 199.0	530.3, 532.2, 533.8*
5AgCl/5Au-D/$SrFeO_3$	367.5, 368.6	84.5, 85.5	199.1, 200.3, 201.0	528.6*, 530.4, 532.3

* indicates minor (<5% total peak area) peaks

† indicates Au 4f$_{7/2}$ peak defined at BE = 84.00 eV, as used for calibration of all other measurements.

S6. Particle size distributions from SEM images

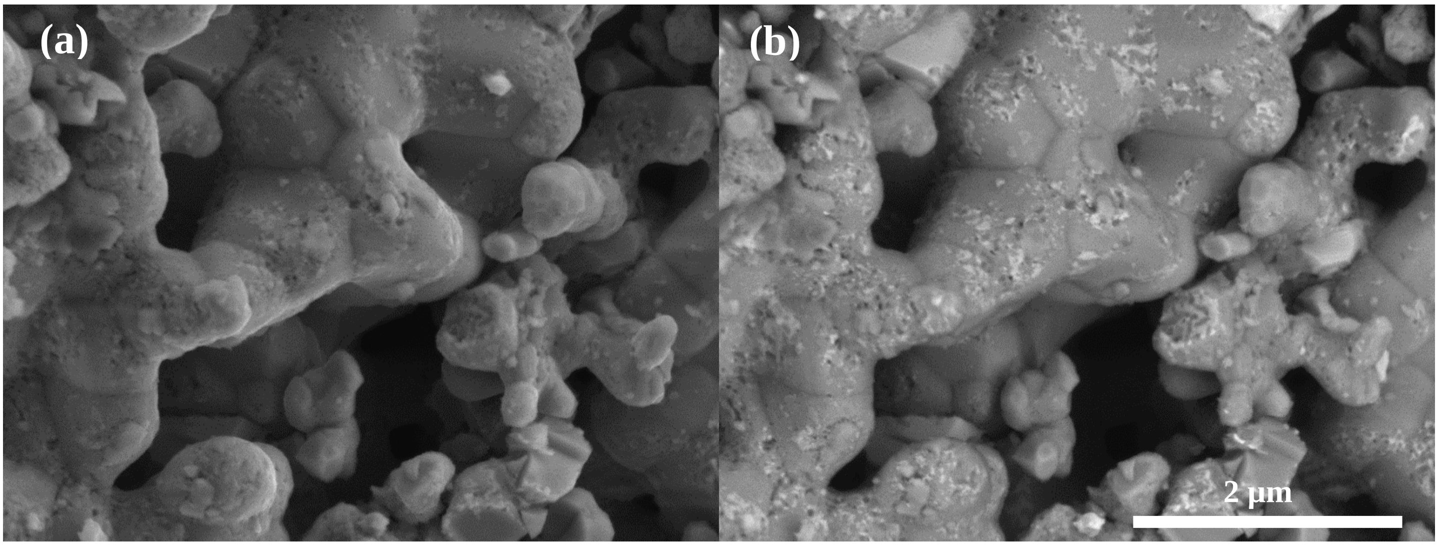

Figure S6: SE **(a)** and BSE **(b)** SEM micrographs, Ag/SrFeO$_3$ particles, showing small distinct Ag particles at the surface.

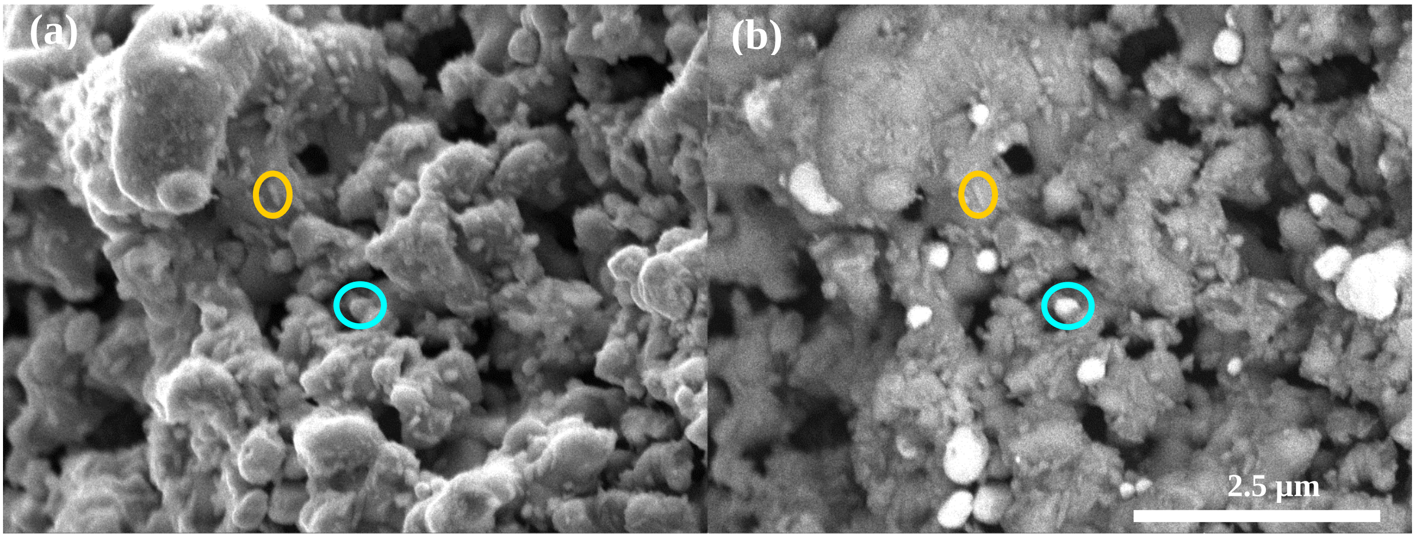

Figure S7: SEM secondary electron **(a)** and back-scattered electron **(b)** micrographs of 5Ag/5Au-D/SrFeO$_3$, with circled areas corresponding to the different particle morphologies observed. Orange = AgCl, blue = AgAu.

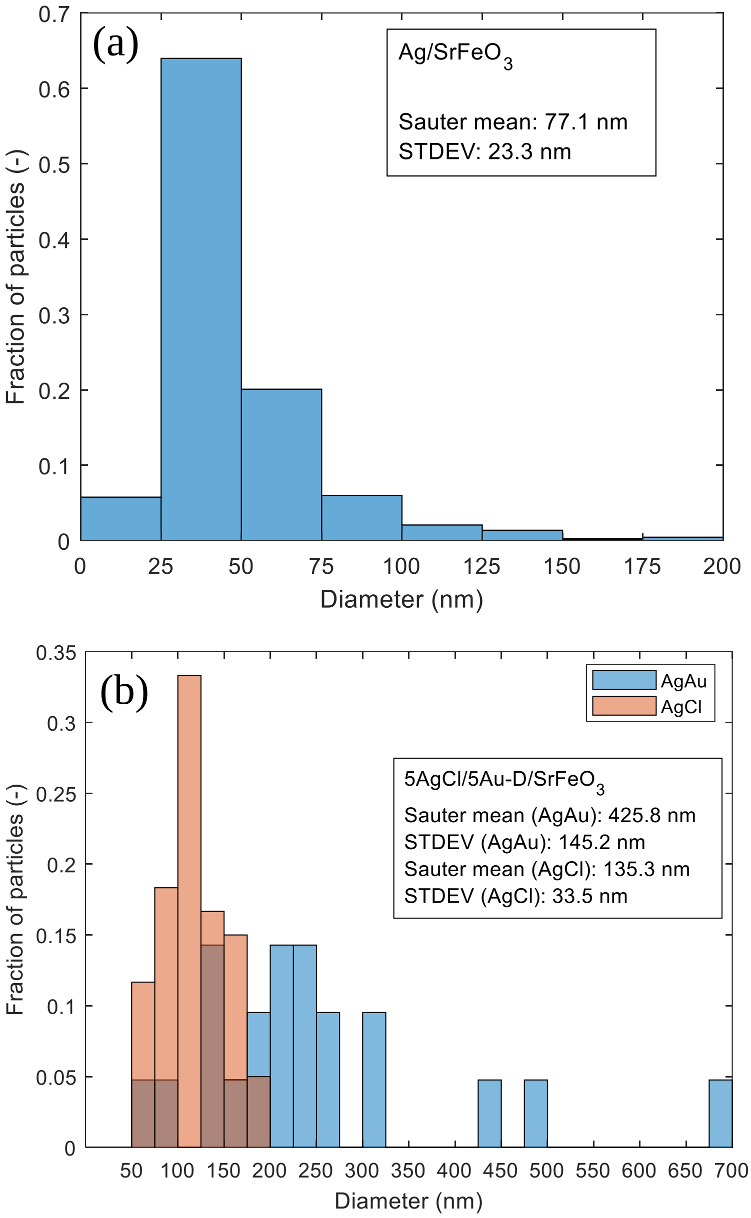

Figure S8: Particle size distributions for **(a)** Ag/$SrFeO_3$ and **(b)** 5AgCl/5Au-D/$SrFeO_3$ samples, measured from SEM images (n = 433 for Ag/$SrFeO_3$; n = 81 for 5AgCl/5Au-D/$SrFeO_3$).

S7. Reactor outlet compositions for reactions over *x*AgCl/*(10-x)*Au-D/$SrFeO_3$ samples, and estimation of adsorbed and dissolved oxygen in catalysts

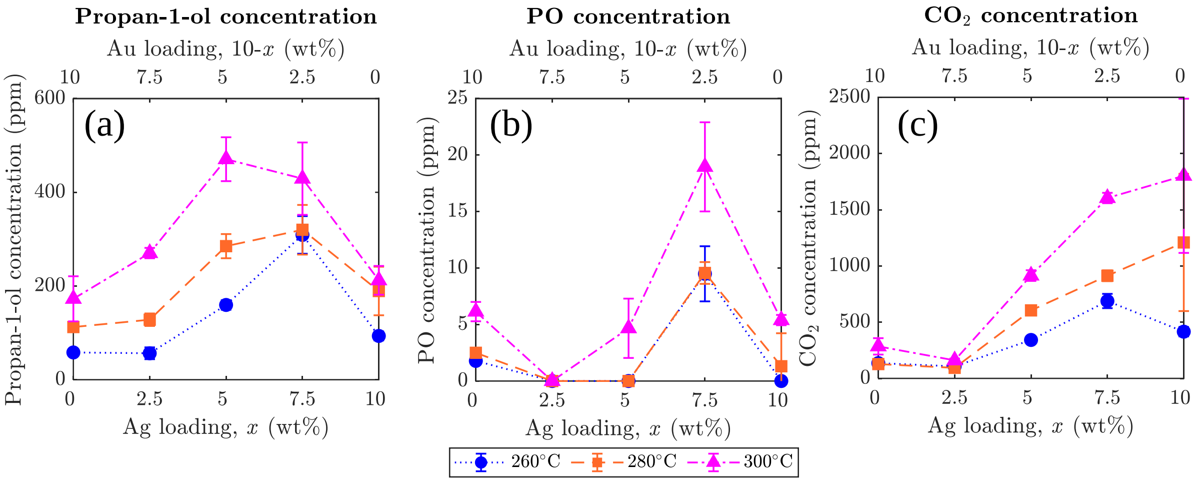

Figure S9: Average outlet concentration of **(a)** propan-1-ol, **(b)** PO, and **(c)** CO_2 for *x*AgCl/(*10-x*)Au-D/$SrFeO_3$ samples. Error bars show standard deviation over 5 cycles. Lines only for guidance.

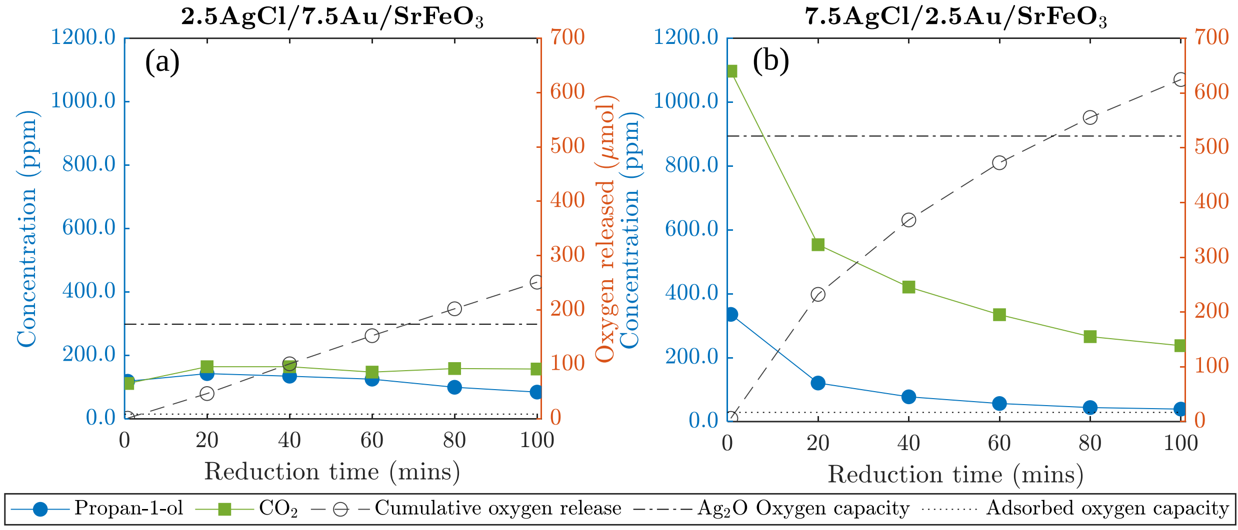

Figure S10: Graphs showing outlet gas composition for extended reduction of **(a)** 2.5AgCl/7.5Au-D/$SrFeO_3$ and **(b)** 7.5AgCl/2.5Au-D/$SrFeO_3$ in 5.13 vol% propylene at 280ºC. Horizontal lines indicate calculated oxygen availability from Ag_2O if all Ag were present as Ag_2O, and available oxygen from surface adsorption at the catalyst.

Extended reduction was performed over 2.5AgCl/7.5Au-D/$SrFeO_3$ and 7.5AgCl/2.5Au-D/$SrFeO_3$ catalysts by passing propylene over the active bed for 100 min, taking a gas sample from the outlet stream every 20 min. Rate of oxygen release is indicated by the gradient of the curve corresponding to cumulative oxygen release. For 2.5AgCl/7.5Au-D/$SrFeO_3$ (Fig. S10a), the gradient is approximately constant, indicating a constant rate of oxygen release. For 7.5AgCl/2.5Au-D/$SrFeO_3$ (Fig. S10b), the cumulative oxygen release plateaus with increasing time, corresponding to a decrease in the rate of oxygen release.

Maximum possible oxygen available from silver oxides in the hypothetical case that all Ag was present as Ag_2O was estimated using

$$n_{Oxygen} = \frac{m_{bed} w_{Ag}}{2M_R(Ag)} \qquad \textbf{[Eq. S2]}$$

where n_{Oxygen} is the amount of oxygen available (mol), m_{bed} is the mass of the active bed (*i.e.* 1.5 g for all experiments), w_{Ag} is the nominal mass fraction of surface Ag, and $M_r(Ag)$ is the molar mass of silver (g/mol). The factor of 2 in the denominator accounts for the 2:1 ratio of Ag to O in Ag_2O.

The maximum theoretical adsorbed oxygen at the surface of AgCl was estimated by assuming a Sauter mean diameter, $d_{3,2}$, of 135.3 nm (as estimated from SEM images), and assuming approximately spherical AgCl particles. Oxygen was assumed to adsorb as $(O_2)_a$ at surface Ag sites on AgCl [17], with one adsorbed O_2 molecule per four Ag surface sites; oxygen adsorption on AgAu was assumed to be minimal [18,19].

The dispersion of AgCl, *D*, was then estimated from [20]:

$$D = \frac{\rho_s \pi {d_{3,2}}^2}{\rho_b \frac{\pi {d_{3,2}}^3}{6}} = \frac{6\rho_s}{\rho_b}\frac{1}{d_{3,2}} \qquad \textbf{[Eq. S3]}$$

where $\rho_s = 7.03 \times 10^{19}\ m^{-2}$ is the surface atomic density of AgCl averaged over the (100), (110), and (111) planes, and $\rho_b = 4.47 \times 10^{28}\ m^{-3}$ is the bulk atomic density for a lattice parameter of 5.546 Å [21].

The number of moles of adsorbed oxygen atoms is then estimated from

$$O_A = D \times \frac{w m_{cat}}{2M_r} \qquad \textbf{[Eq. S4]}$$

where *w* is the measured AgCl loading (as given in Table S2), m_{cat} is the mass of the active bed and M_r is the molar mass of AgCl. The maximum amount of adsorbed oxygen available was estimated to be ~8 µmol for 2.5AgCl/7.5Au-D/$SrFeO_3$, and ~17 µmol for 7.5AgCl/2.5Au-D/$SrFeO_3$. For 7.5AgCl/2.5Au-D/$SrFeO_3$, the maximum theoretical oxygen available from adsorbed oxygen is of the order of the amount of oxygen detected in products after ~1 min of reduction. As appreciable activity is detected after >20 min of reduction, the contribution of adsorbed oxygen is taken to be minimal, and so oxygen provided from the $SrFeO_3$ support was assumed to be the primary source of oxygen in products. Additionally, Lu and co-workers [4] found that bulk AgCl is not an active catalyst towards oxidation of propylene in gaseous oxygen. Therefore, it is unclear what fraction, if any, of the calculated maximum adsorbed oxygen on supported AgCl would be able to react with propylene. Furthermore, XPS measurements did not detect a characteristic peak for adsorbed or dissolved oxygen on the sample of $AgCl/SrFeO_3$ (Fig. 4), suggesting that the actual amount of adsorbed oxygen may be well below the estimated maximum. The amount of oxygen soluble in AgCl was crudely estimated, taking the specific molar solubility of oxygen in AgCl to be around 16 µmol/g[22]. The maximum amount of oxygen that could be dissolved in AgCl for the $7.5AgCl/2.5Au\text{-}D/SrFeO_3$ sample was estimated to be of the order ~ 1.6 µmol, which is an order of magnitude less than the amount of oxygen detected in products after 1.5 mins of reduction, and so is neglected.

The total absorption and dissolution of oxygen in Au, $O_{Tot,Au}$ was estimated using:

$$O_{Tot,Au} = A_{Au} \cdot \frac{m_{Au}}{\rho_{Au}} \cdot \frac{P}{RT} \qquad \textbf{[Eq. S5]}$$

where A_{Au} is the estimated volumetric oxygen solubility (m^3_{O2}/m^3_{AgAu})[23], m_{Au} is the mass of gold present, estimated from XRD measurements, ρ_{Au} is the density of gold (kg/m^3) [24], P is the pressure (Pa), R is the molar gas constant (J/kg-K) and T is the reaction temperature (K).

The sample with maximum gold loading was $Au\text{-}D/SrFeO_3$, with 7.3 wt% Au loading. The maximum amount of oxygen that could be absorbed by Au in $Au\text{-}D/SrFeO_3$, was estimated to be of the order ~ 1 nmol, *i.e.* several orders of magnitude less than the amount of oxygen detected in reaction products. Therefore, the oxygen absorbed by gold was assumed to be negligible for all other samples with lower gold loading.

The maximum amount of oxygen dissolvable in bulk Ag, $O_{dis,Ag}$ was estimated by using:

$$O_{dis,Ag} = \varphi \frac{m_{Ag}}{M_{R(Ag)}} \qquad \textbf{[Eq. S6]}$$

where φ is the molar solubility of oxygen in Ag (taken to be $\varphi = 10^{-6}$ mol_O/mol_{Ag} [25]), m_{Ag} is the mass of Ag, and $M_{r(Ag)}$ is the molar mass of Ag. For the sample with the highest Ag loading, $Ag/SrFeO_3$, with 11.8 wt% Ag loading, the maximum dissolvable oxygen was estimated to be of the order ~ 16 nmol. As this is at least two orders of magnitude less than the amount of oxygen detected in reaction products, the amount of oxygen dissolved in Ag was taken to be negligible for all other samples with lower silver loading.

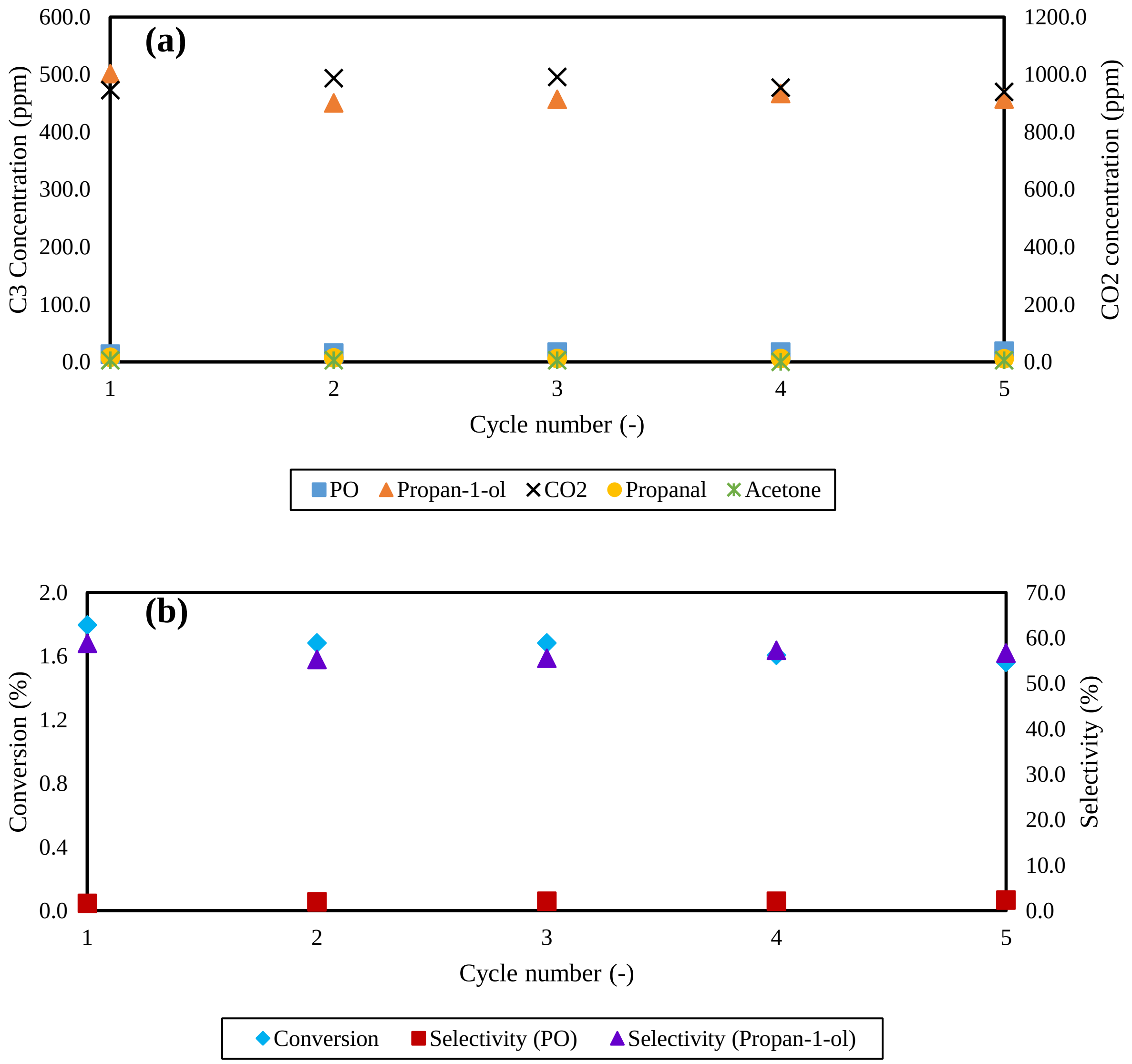

Figure S11: Outlet composition **(a)** and conversion/selectivity **(b)** for Ag-AgCl/Au-H/$SrFeO_3$ over 5 cycles at 280°C, showing minimal change over the course of 5 cycles.

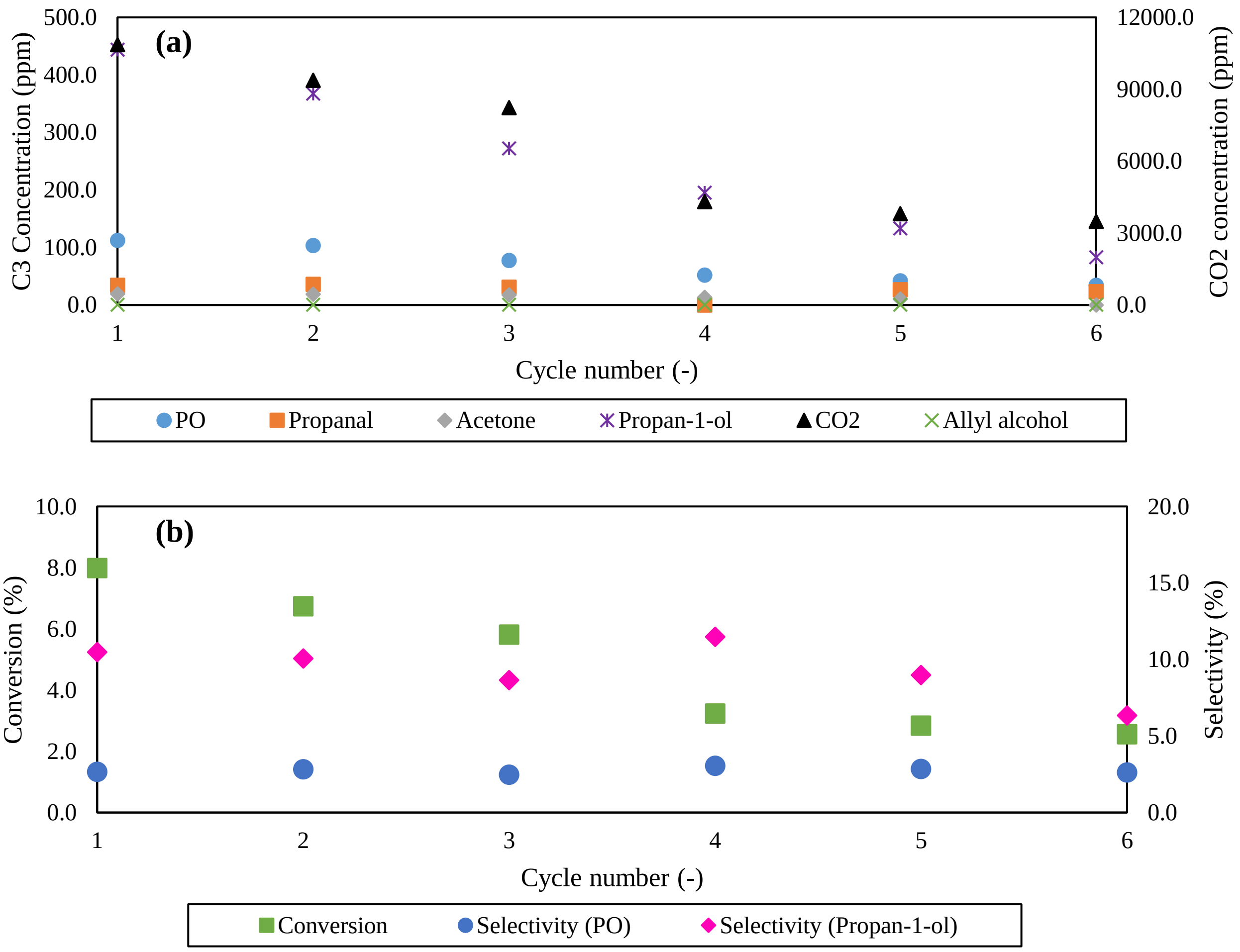

Figure S12: Outlet composition **(a)** and conversion/selectivity **(b)** for Ag/Au-L/SrFeO$_3$ over 6 cycles at 280ºC, showing a marked decrease in catalytic activity.

The effect of altering flowrate of propylene over the active bed during reduction was investigated for reaction over 5Ag/5Au-D/SFO, with results shown in Fig. S13.

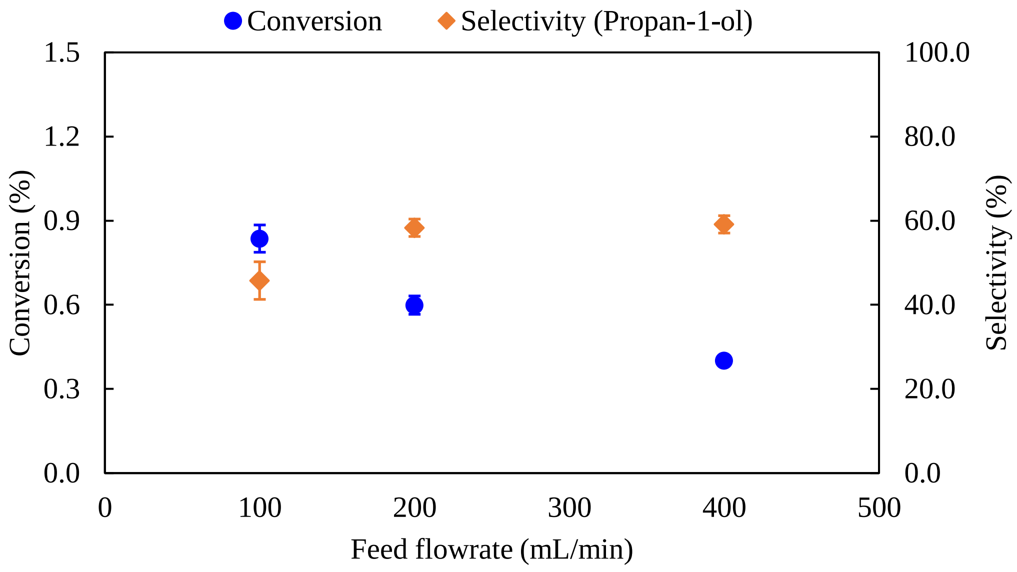

Figure S13: Change in conversion of propylene, and selectivity towards propan-1-ol, over 5Ag/5Au-D/SFO at 260°C, as a result of varying inlet flowrate. Error bars indicate standard deviation over three redox cycles.

S8. Reaction of propylene over Ag/Al_2O_3, AgCl/Au-D/Al_2O_3, and unimpregnated $SrFeO_3$

To verify the postulated chemical looping mechanism, cycling experiments were performed over various control samples. In Fig. S14, CO_2 was the only reaction product for looping over unimpregnated $SrFeO_3$, with extent of complete combustion increasing with increasing temperature. Therefore, the catalyst support was shown to be inactive towards selective oxidation, and as such, that C_3 oxygenate products form at the Ag/Au catalysts. Co-feeding propylene and air 2.5 mol% propylene, 11.5 mol% O_2) over $SrFeO_3$ resulted in formation of CO_2 only, with a decrease in activity from *c*. 1.9% to 0.5% for the overall propylene conversion after 1 h on stream (shown in Fig. S15). Additionally, co-feeding over Ag/$SrFeO_3$ was also performed, giving CO_2 as the only reaction product, in line with previous work on direct propylene oxidation over Ag [26]. The increase in CO_2 between unimpregnated $SrFeO_3$ and Ag/$SrFeO_3$ is attributed to the reaction of propylene with O_a on Ag resulting in enhanced combustion *via* stripping of the hydrogen atom bonded to the γ-carbon in propylene to form an unstable allyl radical, as compared to reaction of propylene with $SrFeO_3$ lattice oxygen.

Samples of Ag and AgCl/Au-D catalysts impregnated on particles of α-Al_2O_3 (180-355 µm, Alfa Aesar) were prepared by incipient wetness impregnation as described in the main manuscript. Reaction of propylene over Ag/Al_2O_3 and 5AgCl/5Au-D/Al_2O_3 under looping conditions was investigated, as shown in Fig. S16. For both samples, CO_2 was detected as the only reaction product, indicating that reaction between propylene and adsorbed surface oxygen or AgO_x phases was not selective in the absence of the $SrFeO_3$ oxygen carrier support. The rapid decrease in CO_2 concentration for Ag/Al_2O_3 was attributed to the depletion of AgO_x phases, which were not subsequently regenerated during the re-oxidation step.

Finally, a sample of AgCl supported on porous γ-Al_2O_3 (212-425 µm, Alfa Aesar), was prepared by incipient wetness impregnation and subsequent addition of hydrochloric acid, as described in the main manuscript (XRD pattern shown in Fig. S17). Reaction of propylene over the AgCl/γ-Al_2O_3 under chemical looping conditions was investigated, with no products containing oxygen (including CO_2) detected above 5 ppm. Therefore, the contribution of oxygen adsorbed on or dissolved in AgCl to formation of oxygenated products was considered to be negligible in all other chemical looping experiments.

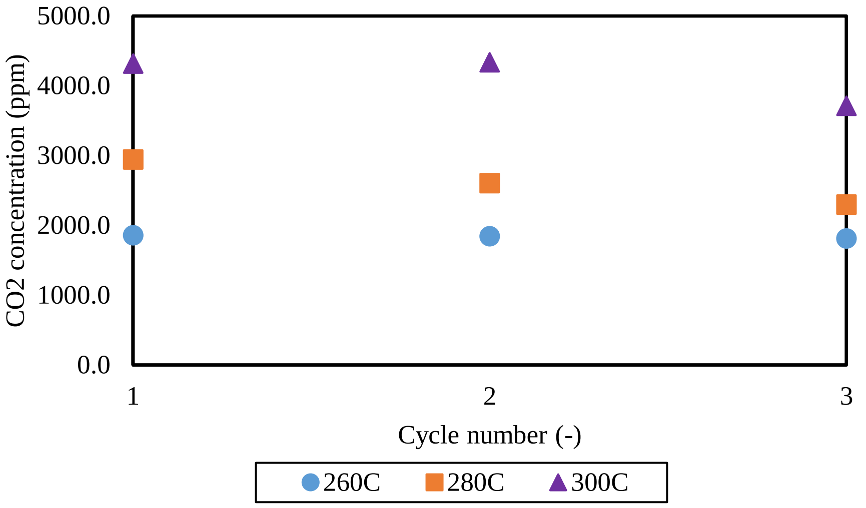

Figure S14: Graph showing outlet composition for propylene cycling over unimpregnated $SrFeO_3$. No other reaction products above 5 ppm were detected.

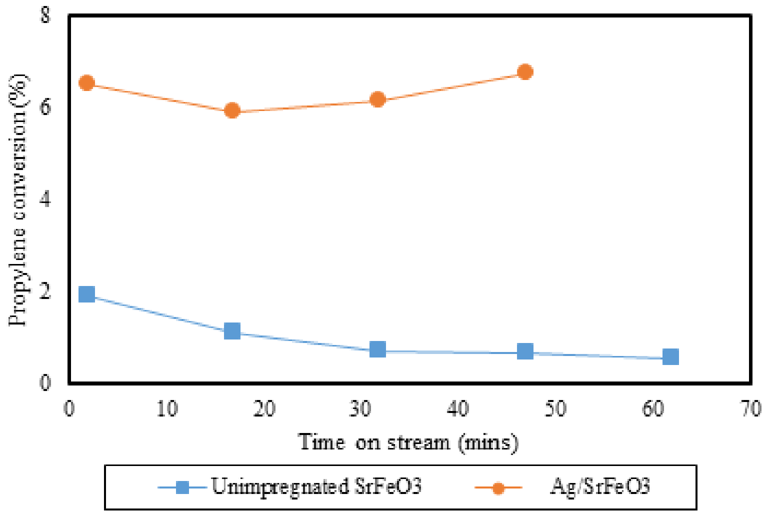

Figure S15: Graph showing propylene conversion for co-feeding of propylene (100 mL/min) and air (100 mL/min) over unimpregnated $SrFeO_3$, and $Ag/SrFeO_3$. The only detected reaction product was CO_2.

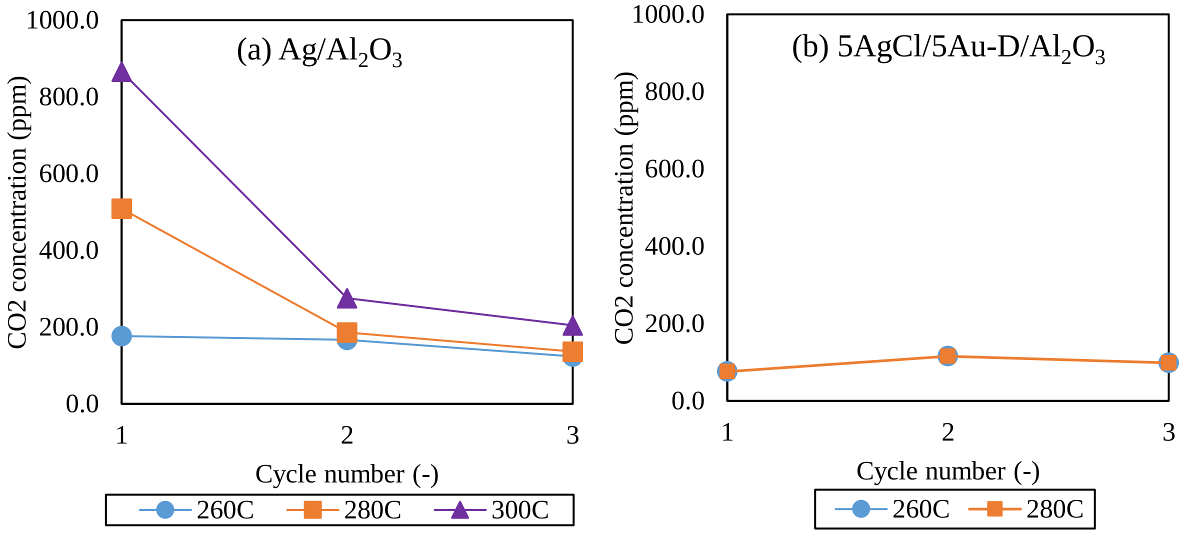

Figure S16: Graphs showing outlet composition for propylene cycling over **(a)** Ag/Al_2O_3 and **(b)** $5Ag/5Au\text{-}D/Al_2O_3$. No other carbon-containing reaction products above 5 ppm were detected.

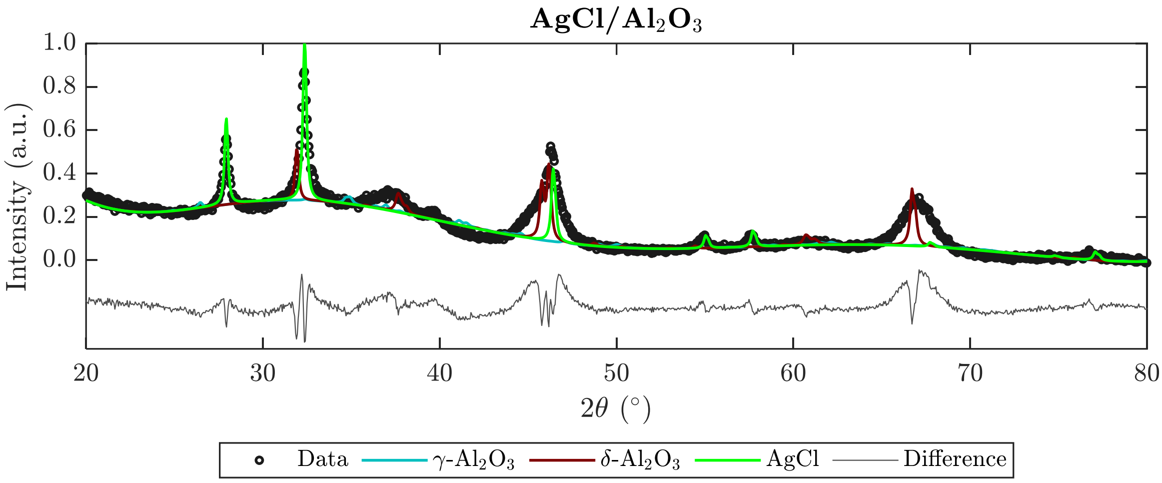

Figure S17: XRD pattern for AgCl impregnated on γ-Al_2O_3, showing considerable peak broadening, thus indicating nanoparticles of AgCl as the dominant phase containing Ag. The main alumina phase was also found to be δ-Al_2O_3 rather than γ-Al_2O_3 as a result of the preparation procedure.

S9. Co-feeding H_2O and H_2 with propylene over 7.5Ag/2.5Au-D/SFO

To confirm that propan-1-ol was not formed by hydration of propylene with water, water vapour (2700 ppm) was added to propylene for reduction over 7.5Ag/2.5Au-D/$SrFeO_3$ (with outlet composition shown in Fig. S18). No significant change in propan-1-ol concentration was detected, indicating that the mechanism is unlikely to proceed *via* a reaction between propylene and water. However, a small increase in the concentration of other C_3 products, in particular PO, was detected, possibly indicating a minor promotional effect of H_2O towards epoxidation of propylene [27].

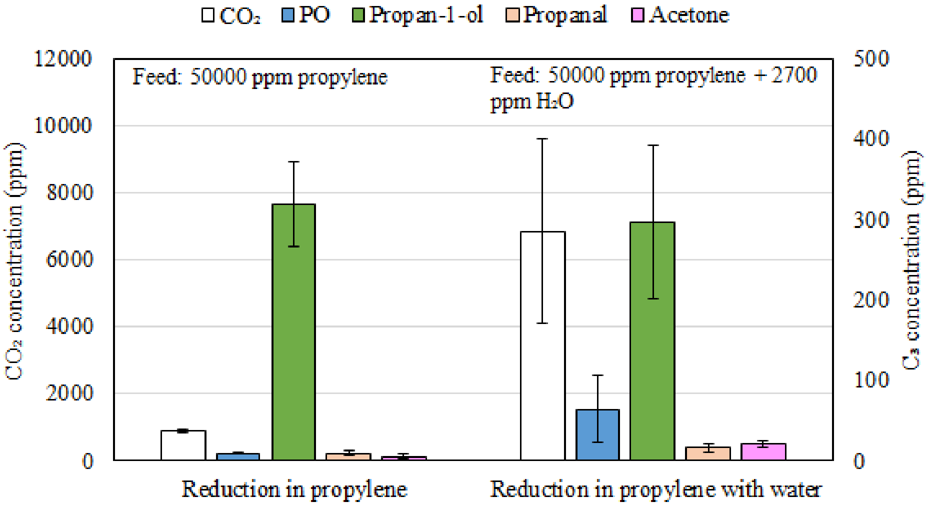

Figure S18: Reaction products for reaction over 7.5Ag/2.5Au-D/$SrFeO_3$, for propylene with and without H_2O added. Error bars indicate standard deviation over three redox cycles.

In order to verify if propan-1-ol is indeed formed from reaction of linear oxametallacycle (OMC) species with gaseous hydrogen, 2500 ppm H_2 was added to propylene for reduction over 7.5Ag/2.5Au-D/SFO, with comparison of outlet products shown in Fig. S19. Concentration of all C_3 oxygenates decreased as compared to the base-case without additional hydrogen, with a marked decrease in propan-1-ol, and a marked increase in the concentration of CO_2. However, conversion of hydrogen was high, at *c.*85%, suggesting that the presence of excess gaseous H_2 resulted in the preferential reaction of H_2 with surface O_a species, or with the $SrFeO_3$ oxygen carrier, to form water. Therefore, the lattice oxygen available to react with propylene to form C_3 oxygenates may have been limited, with reduction of the support resulting in inferior selectivity towards propan-1-ol (as shown in Fig. 6c in the main manuscript).

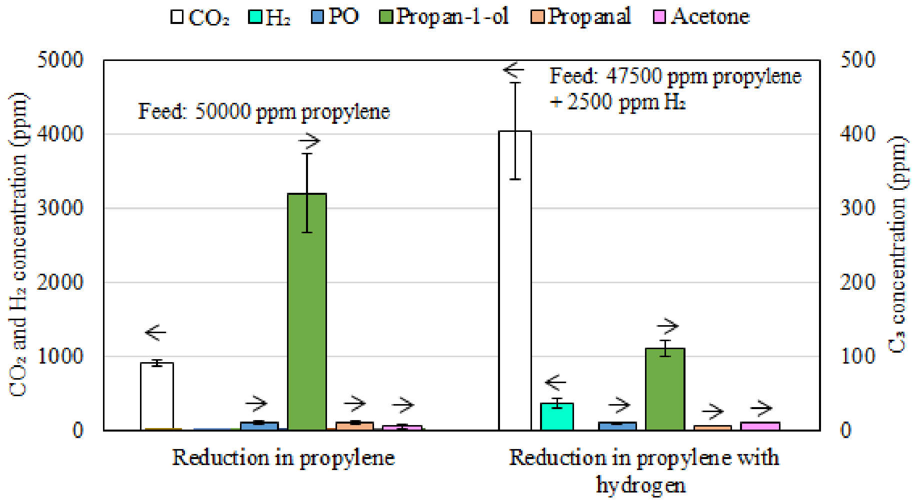

Figure S19: Reaction products for reaction over 7.5Ag/2.5Au-D/$SrFeO_3$, for propylene with and without H_2 added. Error bars indicate standard deviation over three redox cycles.

Supplementary References

1 P. Scherrer, *Nachrichten von der Gesellschaft der Wissenschaften zu Göttingen, Math. Klasse* , 1918, 98–100.

2 M. P. Seah, I. S. Gilmore and G. Beamson, *Surf. Interface Anal.*, 1998, **26**, 642–649.

3 S. W. Gaarenstroom and N. Winograd, *J. Chem. Phys.*, 1977, **67**, 3500–3506.

4 J. Lu, M. Luo, H. Lei and C. Li, *Appl. Catal. A Gen.*, 2002, **237**, 11–19.

5 A. M. Ferraria, A. P. Carapeto and A. M. Botelho do Rego, *Vacuum*, 2012, **86**, 1988–1991.

6 R. J. Chimentão, I. Cota, A. Dafinov, F. Medina, J. E. Sueiras, J. L. G. de la Fuente, J.

L. G. Fierro, Y. Cesteros and P. Salagre, *J. Mater. Res.*, 2006, **21**, 105–111.

7 S. Malathi, T. Ezhilarasu, T. Abiraman and S. Balasubramanian, *Carbohydr. Polym.*, 2014, **111**, 734–743.

8 N. N. Kariuki, J. Luo, M. M. Maye, S. A. Hassan, T. Menard, H. R. Naslund, Y. Lin, C. Wang, M. H. Engelhard and C.-J. Zhong, *Langmuir*, 2004, **20**, 11240–11246.

9 I. Srnová-Šloufová, B. Vlčková, Z. Bastl and T. L. Hasslett, *Langmuir*, 2004, **20**, 3407–3415.

10 H. Falcón, J. A. Barbero, J. A. Alonso, M. J. Martínez-Lope and J. L. G. Fierro, *Chem. Mater.*, 2002, **14**, 2325–2333.

11 A. Abd El-Naser, E. K. Abdel-Khalek, E. Nabhan, D. A. Rayan, M. S. Gaafar and N. S. Abd El-Aal, *Philos. Mag.*, 2020, **101**, 710–728.

12 G. Schön, J. Tummavuori, B. Lindström, C. R. Enzell, C. R. Enzell and C.-G. Swahn, *Acta Chem. Scand.*, 1973, **27**, 2623–2633.

13 V. K. Kaushik, *J. Electron Spectros. Relat. Phenomena*, 1991, **56**, 273–277.

14 J. Lei, J. Dai, K. B. Tan, J. Huang, G. Zhan and Q. Li, *ACS Sustain. Chem. Eng.*, 2021, **9**, 794–808.

15 T. C. R. Rocha, A. Oestereich, D. V Demidov, M. Hävecker, S. Zafeiratos, G. Weinberg, V. I. Bukhtiyarov, A. Knop-Gericke and R. Schlögl, *Phys. Chem. Chem. Phys.*, 2012, **14**, 4554.

16 Y. Qin, Y. Cui, Z. Tian, Y. Wu and Y. Li, *Nanoscale Res. Lett.*, 2017, **12**, 247.

17 S. Kim, S.-C. Lee, C. Lee, M. H. Kim and Y. Lee, *Nano Energy*, 2018, **48**, 134–143.

18 P. Geenen, H. Boss and G. Pott, *J. Catal.*, 1982, **77**, 499–510.

19 S. Rojluechai, S. Chavadej, J. W. Schwank and V. Meeyoo, *Catal. Commun.*, 2007, **8**, 57–64.

20 J. C. Gebers, A. R. P. Harrison and E. J. Marek, *Discov. Chem. Eng.*, , DOI:10.1007/s43938-022-00011-4.

21 M. Rabiei, A. Palevicius, A. Dashti, S. Nasiri, A. Monshi, A. Vilkauskas and G. Janusas, *Materials (Basel).*, 2020, **13**, 4380.

22 A. Jayaraman and R. T. Yang, *Chem. Eng. Sci.*, 2005, **60**, 625–634.

23 F. J. Toole and F. M. G. Johnson, *J. Phys. Chem.*, 1933, **37**, 331–346.

24 J. C. Kraut and W. B. Stern, *Gold Bull.*, 2000, **33**, 52–55.

25 J. Lu, J. J. Bravo-Suárez, A. Takahashi, M. Haruta and S. T. Oyama, *J. Catal.*, 2005, **232**, 85–95.

26 S. J. Khatib and S. T. Oyama, *Catal. Rev.*, 2015, **57**, 306–344.

27 I. D. Charisteidis and K. S. Triantafyllidis, *Catal. Today*, 2020, **355**, 654–664.